ROBOT NAVIGATION

Wireless flow-powered miniature robot capable of traversing tubular structures

Chong Hong[1,2]†, Yingdan Wu[1,2]†, Che Wang[1], Ziyu Ren[2,3], Chunxiang Wang[2,4], Zemin Liu[2,4], Wenqi Hu[5,6]*, Metin Sitti[2,4,7]*

Wireless millimeter-scale robots capable of navigating through fluid-flowing tubular structures hold substantial potential for inspection, maintenance, or repair use in nuclear, industrial, and medical applications. However, prevalent reliance on external powering constrains these robots' operational range and applicable environments. Alternatives with onboard powering must trade off size, functionality, and operation duration. Here, we propose a wireless millimeter-scale wheeled robot capable of using environmental flows to power and actuate its long-distance locomotion through complex pipelines. The flow-powering module can convert flow energy into mechanical energy, achieving an impeller speed of up to 9595 revolutions per minute, accompanied by an output power density of 11.7 watts per cubic meter and an efficiency of 33.7%. A miniature gearbox module can further transmit the converted mechanical energy into the robot's locomotion system, allowing the robot to move against water flow at an average rate of up to 1.05 meters per second. The robot's motion status (moving against/with flow or pausing) can be switched using an external magnetic field or an onboard mechanical regulator, contingent on different proposed control designs. In addition, we designed kirigami-based soft wheels for adaptive locomotion. The robot can move against flows of various substances within pipes featuring complex geometries and diverse materials. Solely powered by flow, the robot can transport cylindrical payloads with a diameter of up to 55% of the pipe's diameter and carry devices such as an endoscopic camera for pipeline inspection, a wireless temperature sensor for environmental temperature monitoring, and a leak-stopper shell for infrastructure maintenance.

INTRODUCTION

Wireless miniature robots have been promising in navigating through confined tubular environments—especially those filled with flowing fluids or gases, such as pipelines of cooling or oil-feeding systems in advanced instruments (*1*), human arteries with blood flows (*2*, *3*), or bronchi with airflows (*4*)—and perform various tasks, such as measuring (*5*), cleaning (*6*), and carrying payloads (*7*). These robots have the potential to improve the way we inspect and maintain critical infrastructure (*1*), conduct environmental monitoring (*8*, *9*), and perform medical procedures (*10*, *11*) because of their compact size and ability to traverse tight spaces that are hard to access using tethered or continuum robots (*1*, *12*–*16*). However, the existing offboard and onboard powering and actuation methods suitable for wireless miniature robots limit the types of tasks they can perform and the environments they can operate in.

Offboard powering and actuation is favorable in wireless miniature robots because it frees up onboard space, allowing the development of robots with body sizes down to 10 μm (*17*). Examples include wireless miniature robots actuated by magnetic fields (*2*, *4*, *18*, *19*), light (*16*, *20*), acoustic waves (*17*, *21*), and temperature (*22*, *23*) to navigate inside tubular structures. The externally powered and actuated robots show great flexibility in terms of programming and controlling, so that they can maneuver through the pipelines using a variety of methods, such as swimming (*17*, *19*, *21*), walking (*19*, *22*, *23*), rolling (*16*, *18*, *19*), crawling (*2*, *18*, *19*), and even climbing (*4*). However, this dependence on external devices for powering and actuating locomotion and function makes them only operational in areas where external energy can be transmitted, limiting their applicable environments. For example, the use of magnetic or radio frequency (RF) actuation may not be suitable for ferromagnetic pipelines, whereas light actuation may not be effective for opaque pipelines. Acoustic actuation may not be suitable for airflows that are low–acoustic transmission substances for acoustic waves. In addition, externally powering and actuating a robot to traverse a lengthy and tortuous pipeline requires the use of either bulky accessories covering the entire pipeline or external accessories following the robot as it moves, which could be challenging or even not feasible.

With onboard powering and actuation units, wireless miniature robots with body sizes at the centimeter scale have been developed. Some of the earliest notable examples include wireless mobile robots powered by rigid batteries (*24*) or structural batteries (*25*–*27*), where the load-bearing components of the robot also serve as an electrical power source (*28*). These centimeter-scale robots can hardly be scaled down to millimeter scale because of the presence of onboard batteries. Microrobots carrying chemical fuels as power sources can navigate inside blood vessels and deliver cargo by using surface reactions to generate propulsion forces (*29*–*31*). The locomotion or functional modules of such robots typically consume most of the available onboard power source, which restricts the duration of operation. This limitation is due to the capacity of the chemical fuels or batteries that power the robot. As a result, such robots can only perform short-term missions before requiring recharging or refueling.

The powering and actuation mechanisms also remain major challenges in the field of in-pipe inspection robots (*32*). Despite various proposed powering and actuation methods for such robots,

[1]State Key Laboratory of Robotics and Systems, Harbin Institute of Technology, Harbin 150080, China. [2]Physical Intelligence Department, Max Planck Institute for Intelligent Systems, 70569 Stuttgart, Germany. [3]School of Mechanical Engineering and Automation, Beihang University, Beijing 100191, China. [4]Institute for Biomedical Engineering, ETH Zürich, 8092 Zürich, Switzerland. [5]Department of Mechanical and Aerospace Engineering, Hong Kong University of Science and Technology, Kowloon, Hong Kong. [6]Bioinspired Autonomous Miniature Robots Group, Max Planck Institute for Intelligent Systems, 70569 Stuttgart, Germany. [7]School of Medicine and College of Engineering, Koç University, 34450 Istanbul, Turkey.
*Corresponding author. Email: wenqi@is.mpg.de (W.H.); sitti@is.mpg.de (M.S.)
†These authors contributed equally to this work.

achieving a sustainable powering mechanism that supports long-distance and long-term navigation during inspection tasks remains difficult, especially in small-scale pipelines with diameters at the millimeter scale. Many of these robots are powered and actuated via tethered electrical cables (*1*, *33*–*42*) or fluid tubes (*15*, *43*–*48*), limiting their usage for long-distance pipeline inspection and rendering them unsuitable for pipelines transporting fluids such as oil and gas. A small number of in-pipe robots incorporate onboard batteries (*49*–*52*) for autonomous navigation, but their operational range is constrained by battery capacity, necessitating frequent recharging. Furthermore, battery-powered in-pipe robots presently remain constrained above a specific centimeter-scale threshold and exhibit limitations in further downsizing. Another type of device known as pipeline inspection gauges (PIGs) has been used in industry. Distinguished from in-pipe inspection robots with active motion controllability, PIGs are typically pushed passively by flow pressure inside liquid- or gas-filled pipelines (*53*–*58*). Consequently, they are deficient in active motion control to undertake complex inspection tasks, notably those demanding bidirectional navigation; have limited compatibility with straight or quasi-straight pipelines; and present the risk of scraping damage against pipe walls during motion. In light of this, we envision that equipping wireless tube millirobots with a self-governing powering and actuation unit that actively uses flow power in a controllable manner could enable them to cover unprecedented distances in tubular structures and perform routine tasks for a long duration, which are challenging for existing robots.

In this article, we propose a wireless millimeter-scale wheeled robot that uses energy from environmental flows to navigate through intricate tubular structures (Fig. 1A). The developed flow-powering module, measuring up to 3 mm in diameter, can convert flow energy into mechanical energy. This module is compatible with diverse flow substances, enabling the robot to navigate through flows of gases and liquids of varying viscosities. The designed miniature gearbox with a high reduction ratio of 2018 enables the robot to transmit the converted mechanical energy into the robot's locomotion system and to amplify the impeller's input torque for efficient propulsion. By using adaptive kirigami design–based wheels, the robot can navigate through various tubular structures, including pipes with changing diameters; S-, U-, and spiral-shaped pipes; and complex three-dimensional (3D) pipes. Magnetic gates integrated into the housing enable the direction of the impeller rotation to be switched by an external magnetic field, allowing the robot's locomotion status to be changed, including moving against/with flow and pausing. Because the robot locomotion remains robust even when carrying payloads of various sizes, different functional modules can be integrated with the robot to achieve visual inspection, wireless temperature measurement, pipeline leak mitigation, and other functions. Our robot addresses the needs of applications that demand long-distance navigation and the ability to perform long-duration tasks within confined tubular structures that are filled with flowing gases or liquids.

RESULTS

Concept and design of the wireless miniature flow-powered robot

Our proposed wireless miniature robot can be powered by the flow field and navigate with or against the flow through complex tubular structures, as shown in Fig. 1A. The design of the robot incorporates three key components: a flow-powering module for making use of flow power, a dual-output miniature gearbox for power transmission, and kirigami soft wheels for adaptive locomotion in complex tubes (Fig. 1, B and C).

The flow-powering module consists of an impeller, a housing, and a tunable magnetic gate (Fig. 1Ci). The configuration of the housing and gate can regulate the flow field, driving the impeller to maintain continuous and unidirectional rotation. The rotation direction of the impeller can be switched by changing the gate position. Although the impeller had a high rotational speed, its output torque was weak. To amplify the output torque and convert the impeller's rotation into robot locomotion, we designed a dual-output miniature gearbox with a high reduction ratio of 2018 and connected its input shaft to the impeller (Fig. 1Cii, fig. S1, and table S1), as detailed in Materials and Methods. Two active wheels mounted on the symmetric output shafts of the gearbox rotated at the same speed but in opposite directions, generating propulsion for stable locomotion that allows the robot to traverse tubes predictably without losing balance or traction. This dual-active-wheel setup provided evenly distributed tractions, reducing slippage risk and ensuring better balance on varying diameter pipelines while offering propulsion redundancy, thus increasing overall reliability. Another six passive wheels, together with the two active wheels, are evenly mounted on the robot in a four-front–four-rear layout to support the robot body in the tube (Fig. 1B). All eight wheels adopt compressible kirigami design for adaptivity to tubular structures of complex shapes (Fig. 1Ciii). The developed robot can navigate against the flow in an 11-m sinuous silicone rubber pipeline for more than 10 hours, as shown in Fig. 1D and movie S1, thus illustrating the potential of the proposed flow-powering mechanism to address powering challenges in long-distance pipeline inspection robotics.

Impeller and housing design for efficient flow energy conversion

We considered an impeller design featuring a rectangular fin cross section to ensure consistent performance for clockwise (CW) and counterclockwise (CCW) rotation, as shown in Fig. 2A. The impeller design parameters include the number of fins N_{fin}, fin length l_{fin}, fin height h_{fin}, fin thickness t_{fin}, impeller diameter D_{i}, and impeller height H_{i}. The housing design parameters include housing width w_{house} and opening width w_{open} (Fig. 2B), from which the opening ratio is calculated as

$$r_{\mathrm{open}} = w_{\mathrm{open}} / w_{\mathrm{house}} \quad (1)$$

To evaluate the effect of the abovementioned parameters on the energy conversion performance and thus guide the flow-powering module design, we conducted numerical simulations (Fig. 2B and fig. S2), as detailed in Materials and Methods. The mean impeller rotational speed $\overline{n_{\mathrm{i}}}$ served as the metric for evaluating performance. For the same flow rate and load torque, a higher impeller speed not only means a higher output power of the flow-powering module but also indicates a faster velocity of the robot during pipeline traversal. We validated our simulation model by experimentally characterizing the impeller rotational speed of flow-powering modules with various designs under different load torques and water flow rates (Fig. 2C, fig. S3, and movie S2), as detailed in Materials and Methods. The mean impeller rotational speeds for different values of N_{fin} and l_{fin}, obtained from both simulations and experiments, are presented in

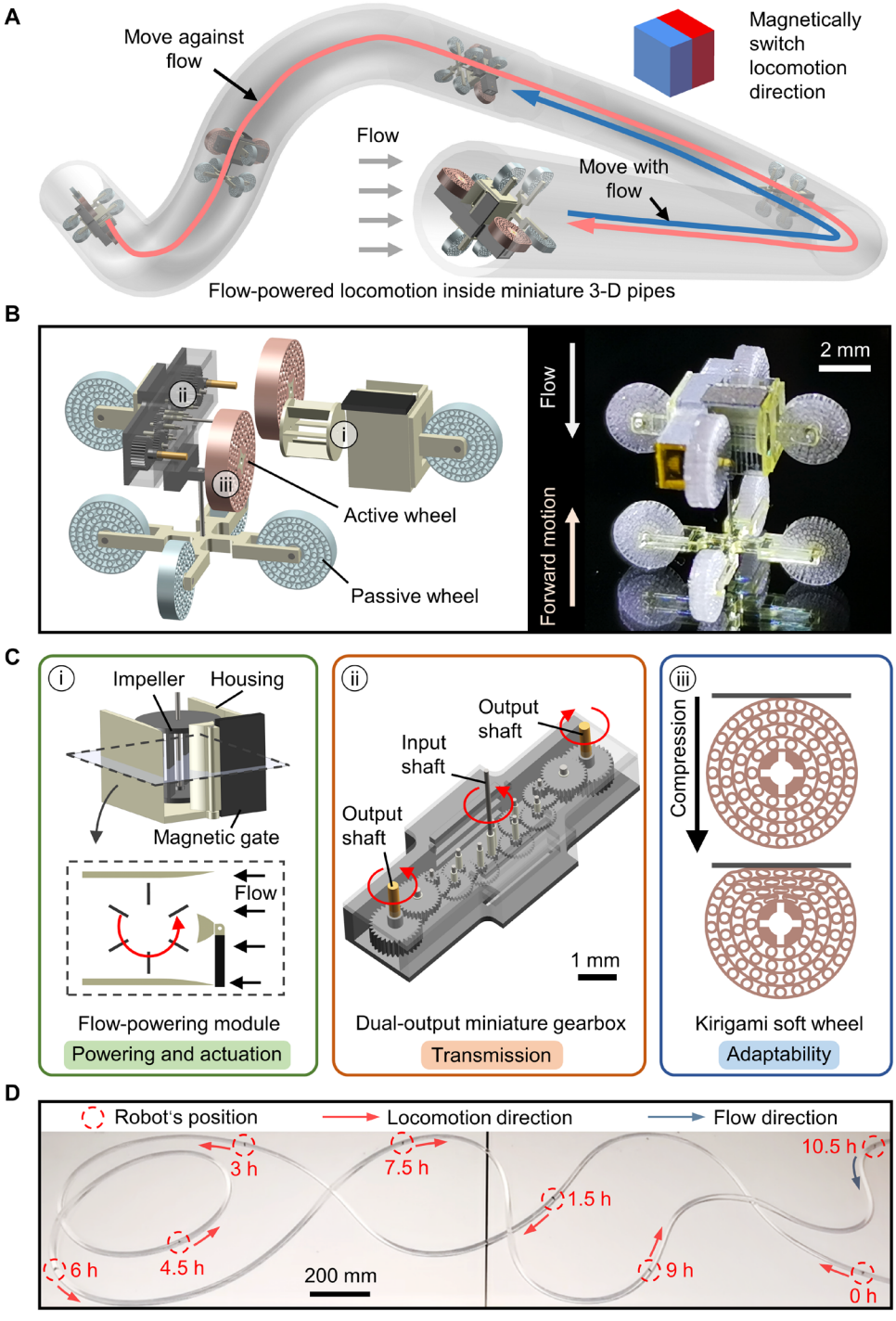

Fig. 1. The wireless miniature flow-powered tube robot capable of navigating complex tubular environments. (**A**) Conceptual schematic depicting the energy-autonomous adaptive locomotion of the robot inside complex 3D pipes filled with flow. (**B**) Design and photographic image of the flow-powered miniature tube robot. (**C**) Design of key modules for the energy-autonomous adaptive locomotion. (i) The flow-powering module converts the flow energy to impeller rotational kinetic energy. Adjusting the gate position can change the rotation direction of the impeller. (ii) The dual-output miniature gearbox with a reduction ratio of 2018 converts the high-speed impeller rotation into a powerful rotation of the two active wheels. (iii) Compressible kirigami wheels for body supporting, anchoring, and adaptive locomotion. (**D**) Robot locomotion against a water flow of 0.44 m/s in an 11-m-long sinuous silicone rubber pipeline featuring an inner diameter of 11.0 ± 0.2 mm. The number after the ± symbol represents the SD. The mean and SD were determined from five measurements using a digital caliper.

Fig. 2D. The computed impeller speeds aligned with experimental data trends despite their numerical overestimation. The discrepancy could be attributed to the presence of the tiny air bubbles adhered to the impeller surface or the underestimated load torque on the impeller shaft due to assembly defects.

We used the simulation model to investigate the effect of the impeller and housing design parameters on impeller speed to guide the flow-powering module design for the robot. First, the housing design of w_{house} and r_{open} was studied with an N6-L0.6 (N6-L0.6 represents an N_{fin} of 6 and an l_{fin} of 0.6 mm) impeller (Fig. 2C). Given the positive correlation between conversion performance and the volume of flow that the module can accommodate, w_{house} was set to its upper limit of 2.74 mm, which was constrained by the robot size. $\overline{n_i}$ is plotted as a function of r_{open} in fig. S2D, reaching its maximum, 9412.7 revolutions per minute (rpm), at r_{open} = 40%.

We then investigated the effect of impeller design parameters on the energy conversion performance using a fixed w_{house} value of 2.74 mm and r_{open} value of 40%. As shown in Fig. 2E, i and ii, both fin thickness t_{fin} and fin-housing gap had a monotonic decreasing effect on the mean impeller rotational speed $\overline{n_i}$ of N6-L0.6 impellers. Specifically, when the gap was fixed at 50 μm, $\overline{n_i}$ decreased from 10367.7 rpm to 7473.3 rpm as t_{fin} increased from 30 to 210 μm (Fig. 2Ei); when t_{fin} was fixed at 30 μm, $\overline{n_i}$ decreased from 10367.7 to 4298.1 rpm as the gap increased from 50 to 300 μm (Fig. 2Eii). Because of fabrication and assembly limits, we chose a t_{fin} value of 60 μm and a gap value of 130 μm for our impeller, which were the lower bounds of their respective ranges. With these values, D_i measures 2.48 mm.

The effects of N_{fin} and l_{fin} on the impeller speed were coupled, nonmonotonic, and dominant (Fig. 2Eiii). In open flow conditions, two aspects must be balanced for efficient flow energy conversion: sufficient propulsion from the flow to the fins for overcoming the impeller load torque and appropriate flow resistance of the impeller during rotation. Increasing either N_{fin} or l_{fin} increased flow resistance, resulting in less flow entering the housing (fig. S2B). However, decreasing N_{fin} or l_{fin} reduced the effective fin area that took propulsion from the flow (fig. S2B). After

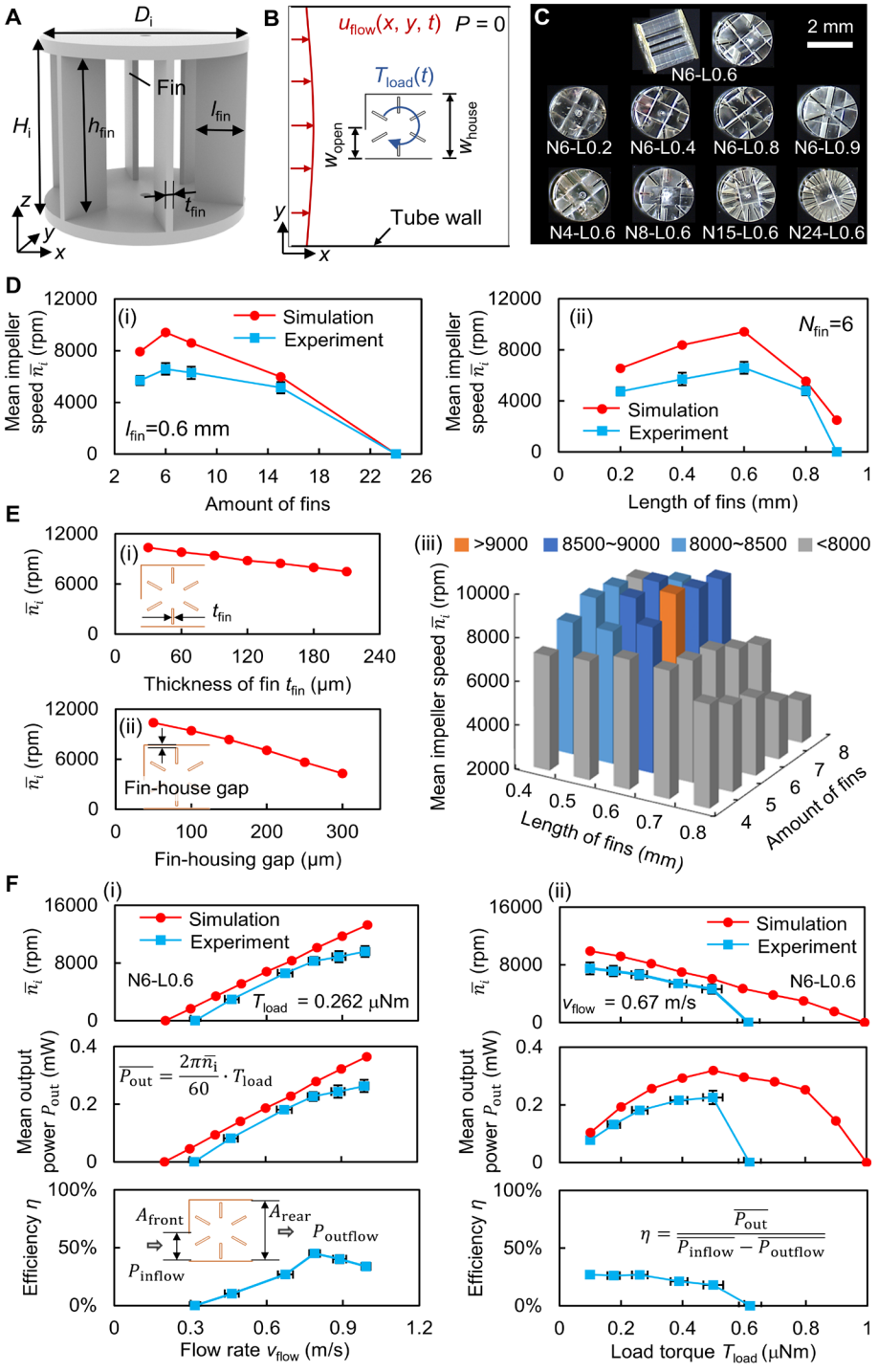

Fig. 2. Simulation and performance characterization of the flow-powering module. (**A**) Impeller design with rectangular fin cross section. (**B**) 2D finite element model and boundary conditions of the selected pipe cross section for simulation. Housing opening ratio r_{open} was calculated by dividing opening width w_{open} by interior width w_{house}. (**C**) Fabricated impellers with different design parameters were used for characterization. The impeller labeled N6-L0.8 has a fin amount of 6 and fin length of 0.8 mm. (**D**) Comparison of simulated and experimental mean impeller rotational speed with different (i) fin amount and (ii) fin length. The flowing medium is water. The average flow rate and load torque for simulations and experiments are 0.67 m/s and 0.177 μN · m, respectively. Error bars represent SD ($N = 5$). (**E**) Simulated mean impeller rotational speed as a function of (i) fin thickness, (ii) fin-housing gap, and (iii) fin amount and fin length. (**F**) Comparison of the simulated and experimental mean impeller rotational speed, output power, and energy conversion efficiency with different (i) flow rate and (ii) load torque. The impeller labeled N6-L0.6 was selected for simulations and experiments. Error bars represent SD ($N = 5$).

conducting a simulation-based parametric sweep study, the N6-L0.6 impeller achieved a highest speed of 9412.7 rpm and was adopted for the robot (Fig. 2Eiii). Although the N6-L0.5 and N7-L0.5 impellers also achieved speeds above 8500 rpm, the smaller fin length caused fluctuation in the rotation speed (fig. S2C). Notably, our miniature impeller design differed from the giant ones used in industry that feature many more and shorter fins (*59*). The many more and shorter fins were designed to work with closed and well-regulated flows that were confined within the energy conversion module for energy conversion, whereas our module must function in open flow conditions where most fluid flow remained external to the impeller-housing module. This difference shaped our impeller-housing module's design, necessitating the accommodation of sufficient flow into the housing while harnessing this flow to effectively drive the impeller for energy conversion. Hence, the scaled-down versions of the industrial impellers were less efficient than our designs in open flows (Fig. 2Eii).

To analyze the performance of the flow-powering module with selected parameters at different flow rates and load torques, we carried out simulations and characterizations (Fig. 2F). The mean impeller rotational speed and output power increase with increasing flow rate, whereas the energy conversion efficiency first increases to its peak of 45.0% at a flow rate of 0.8 m/s and then decreases, as shown in Fig. 2Fi. Our flow-powering module (3 mm by 2.5 mm by 3 mm) achieved an impeller speed of 9595.1 rpm under a load torque of 0.262 μN · m when the average flow rate reached 1.0 m/s, resulting in an output power of 0.263 mW (power density of 11.69 μW/mm^3) and an efficiency of 33.7%. As the load torque increased, the impeller speed decreased monotonically to zero, whereas the output power first increased and then decreased, with a peak value of 0.226 mW occurring at the load torque value of 0.5 μN · m (Fig. 2Fii). Meanwhile, the efficiency ranged between 18.0 and 27.0% with load torques not exceeding 0.5 μN · m. However, there was a discrepancy between the simulation and experimental results when the load torque was larger than 0.5 μN · m. The observed difference can be attributed to the method of applying load torques. In simulation, the torque was applied with a ramping function, whereas in characterization, the torque was present from the beginning. As a result, the impeller had to overcome a much larger torque because of the static friction in the experimental setting, leading to a larger reduction in speed and output power compared with simulations.

Kirigami wheel for adaptive locomotion

We considered a wheel design that can adapt to complex-shaped and varying-diameter tubular structures. This design aims to achieve effective navigation through pipelines of different sizes and surface conditions while maintaining consistent contact and traction with the pipeline wall. To achieve these goals, we proposed the following design principles: The wheel must be able to roll while being compressed to a large extent, which is essential for adaptive locomotion; the wheel should provide sufficient normal force to ensure effective traction that balances fluid drag and prevents slippage; the normal force acting on the wheels during rolling should vary as smoothly as possible to ensure stable locomotion. Our wheel design features a kirigami structure that comprises four layers of ring-shaped units (Fig. 3A). These units enable the wheel to undergo large-scale uniaxial compression without buckling under load, ensuring consistent contact with the surface it rolls on. The active wheel serves as an example, where the rings are distributed across 30 to 100% of the wheel diameter, and the wheel pattern can be defined by three parameters: the diameter ratio of rings between adjacent layers' (p_d), the thickness-to-diameter ratio of rings (p_t), and the normalized quantity of rings (p_n)

$$p_d = d_i / d_{i-1} \tag{2}$$

$$p_t = t_i / d_i \tag{3}$$

$$p_n = N_i d_i / D_i \tag{4}$$

where d_i, t_i, N_i, and D_i denote the outer diameter, thickness, and quantity of rings and the diameter at the ith layer, respectively.

To investigate the performance of different wheels rolling under compression, we conducted simulations and used the mean value $\overline{F_n}$ and fluctuation rate η_{wheel} of the time-history compression force F_n as evaluation metrics (Fig. 3B), as detailed in Materials and Methods. Here, $\overline{F_n}$ indicates the compressive stiffness of the wheel, and η_{wheel} represents the wheel's stability while rolling under a specific compression Δy. The kirigami structure can enhance the wheel's stability by enabling bending-free compression, facilitating consistent contact with its counterpart for sufficient traction. However, it can also yield slight deviations in contact as the wheel rotates because of uneven compressive stiffness around the wheel's circumference. The fluctuation rate η_{wheel} measures this stiffness variation, representing how consistent it is around the wheel's circumference. We first analyzed the effect of p_d on $\overline{F_n}$ and η_{wheel} and found that there had been a small difference (<7.2%) in $\overline{F_n}$ and that η_{wheel} was consistently low, less than 5%, for different values of p_d (Fig. 3Ci and fig. S4). However, because of the constraints of the mold casting process used for fabrication (detailed in Materials and Methods), a p_d of 1.0 was selected for the practical wheel design. Next, we examined the effect of p_n on the wheel performance (Fig. 3Cii). As p_n decreased from 2.3 to 2.0 or 1.7 at $\Delta y = 0.35$ mm, $\overline{F_n}$ decreased by 19 or 41%, whereas η_{wheel} increased from 2.0 to 7.1% or 13.9%. Therefore, our practical wheel design used a high p_n value of 2.3 to maintain a low η_{wheel} level.

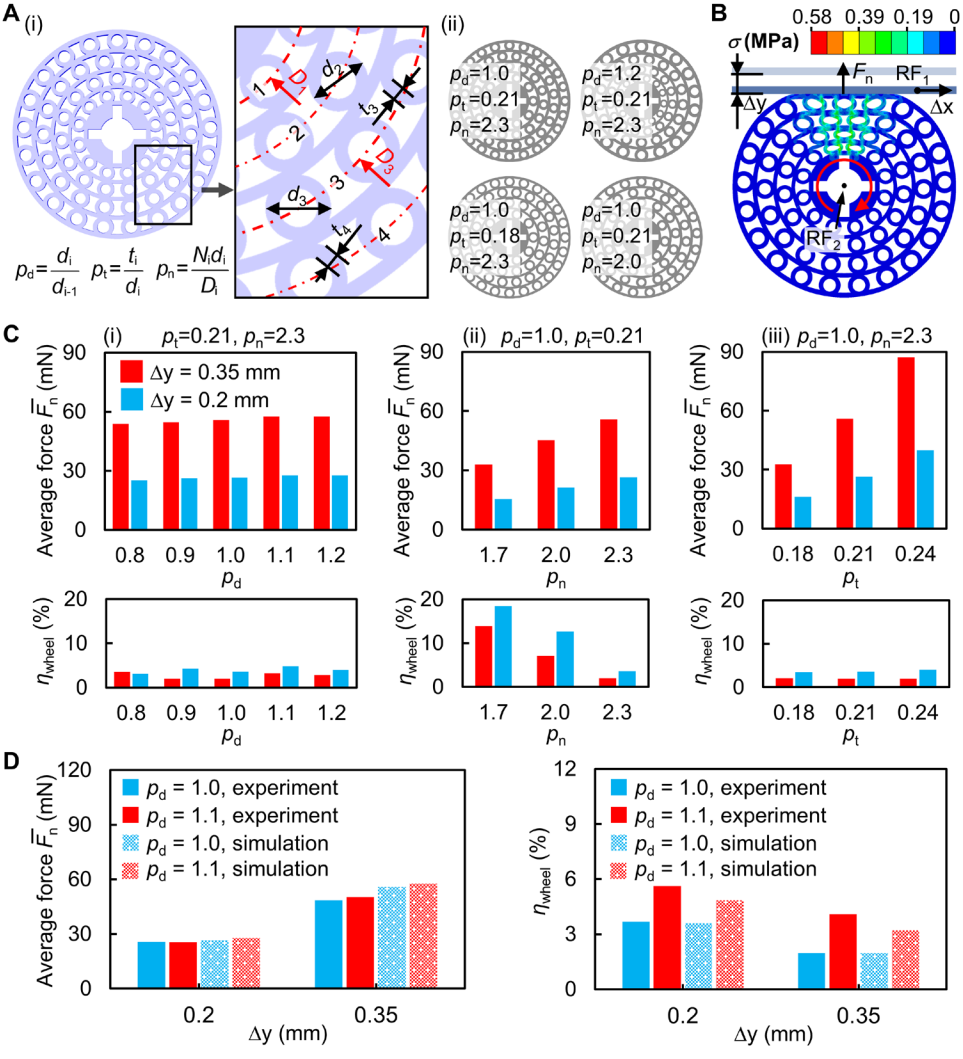

Fig. 3. Design and simulation of the kirigami active wheel for adaptive tubular locomotion. (**A**) Design of the kirigami active wheel. (i) 2D schematic diagram of the wheel with illustration of the design parameters. The number of ring layers i increases from inside to outside. (ii) Wheel configurations with different design parameters. (**B**) Finite element model of a soft wheel and a rigid plate. The plate translated horizontally by a distance Δx after the wheel was compressed vertically by a displacement of Δy. $\overline{F_n}$ and η_{wheel} of F_n during a wheel rotation cycle serve as the evaluation metrics for the wheel's adaptability. (**C**) Influence of wheel design parameters of (i) p_d, (ii) p_n, and (iii) p_t on $\overline{F_n}$ and η_{wheel} at different values of Δy. (**D**) Comparison of simulated and experimental (i) $\overline{F_n}$ and (ii) η_{wheel} under different Δy for wheels with various values of p_d.

Last, we examined the effect of p_t and found that although the difference in η_{wheel} was slight, there was a notable change in $\overline{F_n}$ for different p_t (Fig. 3Ciii). As p_t increased from 0.18 to 0.21 or 0.24 at $\Delta y = 0.35$ mm, $\overline{F_n}$ increased by 171 or 267%. To properly set p_t for our practical wheel, we established an operational criterion: The robot should be able to move upstream in water flow with an average flow rate v_{flow} of up to 0.5 m/s across varying pipe diameters without slippage. A simplified model for the robot's force analysis within a flow-filled pipe was proposed (fig. S5), as detailed in Materials and Methods. Given the positive correlation of F_n with Δy, analysis at the minimum Δy (0.2 mm) was sufficient, aligning with an 11.3-mm-diameter pipe. In this context, within an 11.3-mm-diameter pipe filled with 0.5 m/s water flow, the simulated fluid drag force on the robot, F_{flow}, was 21.02 mN (fig. S5B). With the friction coefficient between polydimethylsiloxane (PDMS) elastomer and diverse materials' lower limit in the presence of water μ_w set as a lower limit of 0.7 (*60*, *61*), F_n should exceed 15.02 mN as per Eq. 12. At $\Delta y = 0.2$ mm, simulated $\overline{F_n}$ values were 16.05, 26.47, and 39.87 mN for p_t values of 0.18, 0.21, and 0.24, respectively. Adequate F_n ensured robust locomotion, given that insufficient F_n lead to slipping, whereas excessive F_n hampered gear transmission efficiency and even damaged the gearbox (*62*). Therefore, we adopted a practical wheel design with a p_t of 0.21 to achieve an appropriate $\overline{F_n}$.

To validate our simulation model for wheel analysis, we conducted characterization on two active wheels of different designs (fig. S6), as detailed in Materials and Methods. The normal force of the wheel under different compressions Δy is plotted as a function of travel distance in one complete rolling revolution in fig. S6E, and the calculated $\overline{F_n}$ and η_{wheel} are reported in Fig. 3D. The wheel with a p_d of 1.0 had a lower η_{wheel} than the one with a p_d of 1.1. For each case, the experimental $\overline{F_n}$ was slightly lower than the simulated one, whereas the experimental η_{wheel} was slightly larger than the simulated one. Fabrication deviations in wheel thickness and inaccurate estimation of material properties can contribute to smaller experimental $\overline{F_n}$. The adhesion between the wheel surface and the test substrate was not considered in the simulation, which could lead to a higher η_{wheel}.

The design of passive wheels is similar to that of active wheels, with one key difference: Passive wheels are fitted with a rigid sleeve in the center to reduce frictional torque because they are not required to transmit torque like active wheels. The structures of both active and passive wheels used by the robot are illustrated in detail in fig. S6F. In addition, we also examined a solid and highly soft wheel with identical dimensions and comparable compressive stiffness to that of the kirigami wheel. However, the solid wheel can buckle during rotation under large compression, as illustrated in fig. S6G.

Motion analysis and demonstration of robot traversing in various environments

With the specific kirigami wheel design, our robot was capable of navigating through complex-shaped varying diameter tubes as demonstrated in Fig. 4A. The active wheels rolled and deformed symmetrically to provide identical propulsion, allowing the robot to traverse straight pipes (Fig. 4A and movie S3). The passive wheels, together with the active wheels, which were evenly distributed in a four-front–four-rear layout, enabled the robot to maintain stable contact in the tube. Because the wheels can anchor and roll properly under large compressions at different scales, the robot can navigate through tubes with diameters ranging from 10.4 to 11.4 mm (Fig. 4Ai). This adaptability allowed the robot to traverse tubes with varying diameters. We demonstrated that the robot can traverse tubes with intermittent or continuous changes in inner diameter while moving in either the direction of or against the flow at an average rate of 0.51 m/s (Fig. 4Aii and movie S3).

We analyzed the locomotion performance of the robot in various water flow conditions, including different flow rates and tube diameters (Fig. 4Aiii). For a given tube diameter, the robot moved faster in both downstream and upstream directions as the flow rate rose (movie S4). At a constant flow rate, the robot exhibited higher speeds when moving with the flow than when moving against the flow because of the presence of fluid drag forces. Specifically, we observed maximum speeds of 1.450 mm/s (0.16 BL/s, where BL represents the robot's body length) in the direction of flow and 0.523 mm/s (0.058 BL/s) against the flow, using a 10.5-mm tube with an average flow rate of 1.047 m/s. There were lower and upper bounds for the flow rates, v_{lower} and v_{upper}, that can drive the robot moving in both directions (Fig. 4Aiii). Beyond a critical flow rate v_{upper}, our experiments revealed that the flow resistance acting on the robot exceeded the maximum anchoring force provided by the wheels, leading to slippage and possible flushing of the robot downstream. Conversely, when the flow rate fell below v_{lower}, the combined effect of gear friction, wheel compression, and damping forces as well as the flow resistance acting on the robot created a load torque that exceeded the available flow torque applied to the impeller, thus hindering the robot's upstream motion. We found that the flow rate range capable of driving the robot expanded from between 0.249 and 0.626 m/s to between 0.395 and 1.047 m/s as the tube diameter decreased from 11.3 to 10.5 mm. We attributed this expansion to an increase in traction force provided by the wheels, which enabled the robot to better resist higher flow resistance. The robot moved against flow with a v_{flow} of up to 0.626 m/s (exceeding our criterion of 0.5 m/s) in glass pipes of different diameters, validating the effectiveness of the robot's force analysis model (Fig. 4Aiii and fig. S5). In addition, we observed an increase in v_{lower} as the tube diameter decreased, which we attributed to the increase in impeller load torque induced by the smaller tube diameter.

In addition to water flows, the robot can also navigate through tubes with flows of other substances. We demonstrated that the robot with the same design can be powered by nitrogen gas and a viscous aqueous solution of glycerol (32.6%, v/v), commonly used as a blood analog (Fig. 4Aiv and movie S5). However, a further optimization of the robot is needed to navigate in a specific flow substance more efficiently because the robot motion performance can be affected by various properties of the flow substances, including the viscosity, solid content, chemicals, and temperature (*63*). The interaction of viscosity, impeller dynamics, and robot motion is complicated. Higher viscosity facilitates impeller drag in the energy conversion module, yet it raises internal friction and energy losses, affecting energy conversion. In addition, fluid drag on the robot body amplifies with viscosity, acting as resistance or propulsion based on motion direction relative to the flow. Substances with solid debris or corrosive/reactive chemicals can damage the impeller and robot, affecting integrity and performance. Extreme temperatures affect impeller-housing and gearbox modules through thermal expansion or contraction. Temperature variations also alter flow viscosity.

Our robot was capable of traversing curved pipes using an adaptive slippage mechanism for its active wheels (Fig. 4B). The mechanism worked differently when the robot navigated the curved pipe in different attitudes. In attitude I, the two active wheels were in the same plane

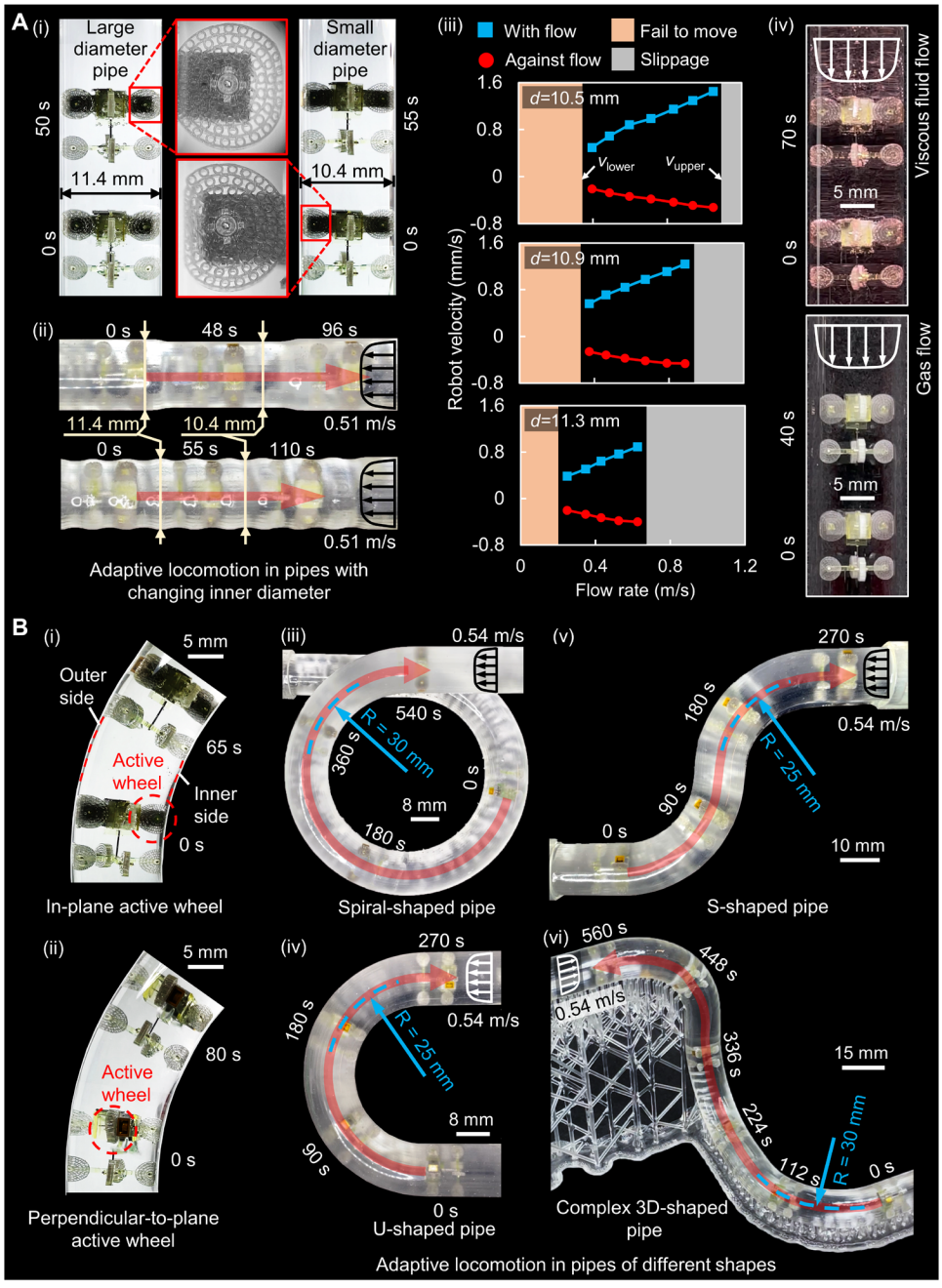

Fig. 4. Analysis and demonstration of adaptive locomotion in various pipes with different flow properties. (**A**) Locomotion analysis in straight pipes of different diameters. (i) The robot can move against the flow in straight glass pipes with diameters ranging from 10.4 to 11.4 mm. (ii) Photographic images of the robot moving through pipes with varying inner diameters that change continuously or intermittently. (iii) Speed characterization at different water flow rates in pipes with diameters of 10.5, 10.9, or 11.3 mm. (iv) Demonstration of the robot locomotion in different flow substances, including nitrogen gas and viscous aqueous solution of glycerol (32.6%, v/v). (**B**) Robot can move against flow in curved glass pipes because of the adaptive wheel slippage at different body attitude cases, when the active wheels were (i) in plane with or (ii) perpendicular to the pipe curvature plane. Demonstrations of the robot navigating (iii) a spiral-shaped pipe with a radius of curvature of 30 mm, (iv) a U-shaped pipe with a radius of curvature of 25 mm, (v) an S-shaped pipe with a radius of curvature of 25 mm, and (vi) a complex 3D-shaped pipe with three segments (the planes of each pipe segment were perpendicular to each other, and the radius of curvature of each pipe segment was 30 mm).

as the curvature of the tubes (Fig. 4Bi). The active wheel at the outer side covered a longer distance than the one at the inner side as the robot made a turn. Because the active wheels were identically driven by the gearbox, the active wheel at the inner side slipped intermittently as it rolled to accommodate the robot turning. In attitude II, the two active wheels were in the plane perpendicular to the curvature of the tubes, so both wheels covered the same distance while the robot turned (Fig. 4Bii). However, slippage can still occur at the active wheels because of misalignment between the active wheel direction and the curvature of the tube. As the active wheels rotated to provide propulsion, the curved tube walls applied asymmetric reaction forces to the passive wheels, resulting in a torque that aligned the robot body with the tube curvature. Therefore, the robot passively turned as it proceeded. The robot locomotion inside complex-shaped tubes usually involved a combination of the mechanisms described above (Fig. 4B, iii to vi). When the robot navigated against the flow in a spiral-shaped tube, it spun slightly about its body centerline in the direction of motion as it moved forward (Fig. 4Biii and movie S6). This spinning motion was due to a combination of factors, such as the surface texture of the pipe, robot assembly errors, and the bending of the wheels. In addition, the robot can navigate against flow in U- and S-shaped in-plane pipes with a 25-mm radius of curvature (Fig. 4B, iv and v, and movie S6). To showcase the robot's ability to move through practical complex tubes, we fabricated a 3D-shaped tube with three segments perpendicular to each other (Fig. 4Bvi). The robot could continuously navigate the tube segments with different attitudes and climb against gravity, demonstrating the robustness of adaptive locomotion (Fig. 4Bvi and movie S6).

Furthermore, our robot showcased the ability to maintain consistent locomotion within pipelines constructed from a wide range of materials, including silicone rubber, copper, stainless steel, polyvinyl chloride (PVC), aluminum, glass, and polymer resin, each of which frequently appears in real-world scenarios involving flow-containing tubes (Figs. 1D and 4, fig. S7, and movie S7). For instance, copper or PVC tubes are prevalent in domestic, laboratory, and industrial plumbing systems

for liquid or gas transportation. Stainless steel or aluminum tubes find frequent use as cooling pipelines in critical setups such as aircraft engines. Soft silicone tubes, because of their flexibility, are often used in laboratory settings, such as cooling or feeding pipelines for customized setups. Despite these variations, the robot's performance remained steady and free from slippage, as indicated by close robot velocity under the same average flow rate in fig. S7B, underlining the robot's versatility and adaptability across different pipeline compositions and a wide range of practical scenarios.

Motion control of the robot

To actively control the locomotion direction of the robot, we equipped the flow-powering module with switchable magnetic gates that can modulate the direction of the impeller rotation through external magnetic control. By adopting a design of the single magnetic gate (Fig. 5Ai and movie S8), the impeller can be driven in two modes, CW and CCW rotation, at different gate positions. Gate position control can be achieved by using the gradient force generated by the proximity of a permanent magnet or by using the magnetic torque generated by the rotation of a permanent magnet (fig. S8). The gate position can be maintained by fluid resistance with the external magnetic field removed. Such a design has the merit of simple control, allowing the robot to reciprocate automatically inside a straight pipeline between two oscillating permanent magnets (Fig. 5Aii). The robot first moved with the flow to approach an oscillating permanent magnet (Fig. 5Aiii). When the magnetic force acting on the gate was sufficient to overcome the fluid resistance, the gate position was switched, so that the robot moved against the flow. When the robot approached the other magnet, it switched the gate position again, resulting in a reciprocal motion. This design stands as a viable solution to the challenges faced by existing in-pipe robots, particularly when tasked with conducting reciprocal inspections along extensive pipelines, including the intricate long-distance pipelines in laboratory and industrial infrastructures (fig. S7, A and C).

By adopting a design of double magnetic gates, the impeller exhibited three switchable states: stop, CW rotation, and CCW rotation (Fig. 5Bi and movie S8). When the external magnetic field was controlled to close both gates (fig. S8B), no flow could pass through the housing, leaving the impeller at a stop state. When both gates were controlled to one side (fig. S8C), the impeller could achieve CW or CCW rotation. In this way, the robot could realize three switchable locomotion states, as illustrated in Fig. 5Bii, where the robot moved with flow, stopped, and moved against flow sequentially. It is worth noting that each motion state of the robot can be maintained after removing the external magnetic field because the flow resistance applied to the gates is sufficient to overcome the magnetic interaction force between the gates to keep the gate state.

To ensure emergency mobility of the robot in the event of unexpected loss of flow field, we attached a magnetic disk to the impeller (fig. S9). We demonstrated that robot locomotion can be actuated in dual modes through either a flow field or an external rotating magnetic field (movie S9).

Our flow-powering module demonstrated compatibility with diverse locomotion direction control methods, expanding beyond magnetic control. One such method involved an automated gate-switching mechanism for self-regulating reciprocating locomotion, integrating mechanical feedback (fig. S10 and movie S10). The gate of the flow-powering module used a V-shaped configuration, with each end connected to one of the two output shafts through a pair of thread and elastic stripes in series (fig. S10A). During operation, with the initial gate position corresponding to upstream motion, the CW rotation of active wheel 1 wound the thread, stretching elastic stripe 1 and storing energy within it (fig. S10Bi). Simultaneously, the CCW rotation of active wheel

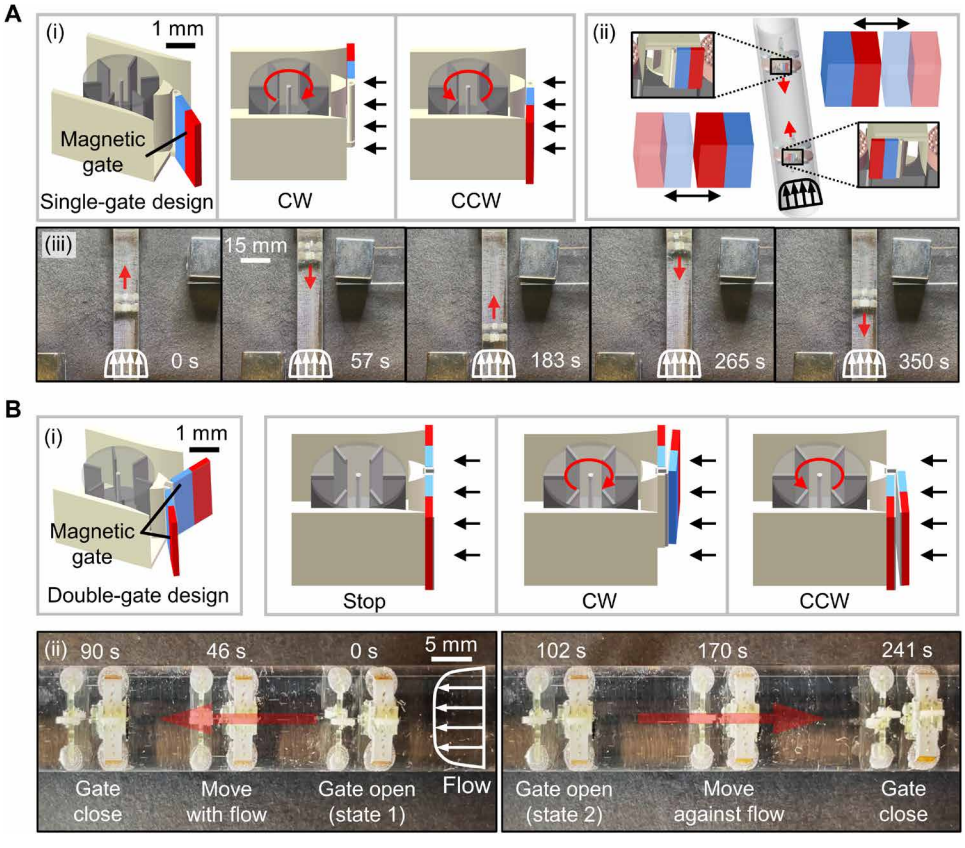

Fig. 5. Modulation of robot locomotion states via external magnetic stimulation. (**A**) Flow-powering module with a single magnetic gate enabled two motion states of the robot. (i) Two different gate positions allowed opposite impeller rotation directions in the same ambient flow field. (ii) Schematic diagram of the setup for automatic reciprocating robot locomotion inside a straight pipeline with reciprocating permanent magnets at two ends of the pipeline. (iii) When the robot approached a reciprocating magnet, the magnetic force changed the gate state, thus switching the robot locomotion direction. (**B**) Flow-powering module with two magnetic gates enabled three motion states of the robot. (i) By closing both gates or opening one gate while closing the other gate, three impeller states can be achieved: stop, CW rotation, and CCW rotation. (ii) By controlling an external magnetic field to sequentially open a gate, close two gates, and open the other gate, the robot can follow flow, pause, and move against flow.

2 released the connected thread, resulting in the relaxation of elastic stripe 2 and its associated torque on the gate. Once the torque exerted by elastic stripe 1 to the gate surpassed the resistance torque generated by the flow, an abrupt gate position shift occurred, redirecting the robot's motion downstream. The robot underwent a similar process to switch from downstream to upstream locomotion (fig. S10Bii). This approach enabled the robot to autonomously engage in self-regulated reciprocating locomotion within the pipeline, requiring no external interventions (fig. S10C). Notably, the reciprocating range of the locomotion is preprogrammable via adjustment of the thread length on both sides of the gate.

Carrier function of the robot while being integrated with miniature tools

By integrating various functional payloads, other tasks can benefit from this energy-autonomous adaptive locomotion platform to function properly inside flow-filled pipelines. The implementation of other tasks depends on additional functional payloads with a nonnegligible volume. To analyze the effect of payload's size on the locomotion performance of the robot, we carried out characterization experiments (Fig. 6A and movie S11). At an average flow rate of 0.46 m/s, the robot carried a cylindrical payload moving against the flow (Fig. 6Ai). Generally, the payload caused a decrease in the robot's speed by 7 to 16%, dependent on its size (Fig. 6A, ii and iii), because the suspended payload resulted in additional fluid drag. For payloads with a constant diameter d_{load} of 6 mm, there was a slight increase in the robot's speed from 0.270 to 0.286 m/s with the increasing payload length l_{load} from 4 to 12 mm (Fig. 6Aii). This is because the drag coefficient of a long cylinder was smaller than that of a short cylinder of the same diameter (*63*). For payloads with a constant l_{load} of 12 mm, the robot's speed decreased from 0.322 to 0.285 m/s as d_{load} increased from 0 to 6 mm (55% of the pipe diameter), and the robot could no longer move when d_{load} exceeded 8 mm (Fig. 6Aiii). The fluid drags increased with the increasing cross-sectional area of a payload. Nevertheless, a proper configuration of the functional payloads can maintain the robot locomotion performance.

The noninvasive monitoring of the temperature of flowing media in pipelines shows promise in promoting pipeline longevity and ensuring the appropriate operation of the system (*64*, *65*). Here, we demonstrated that the robot can carry a wireless miniature temperature sensor (radio-frequency identification, RFID, transponder temperature microchip UCT-2112-24, AnimaLab Inc.) while traversing a pipeline, enabling noninvasive mobile fluid temperature monitoring (Fig. 6B and movie S12). Flow temperature around the robot was measured

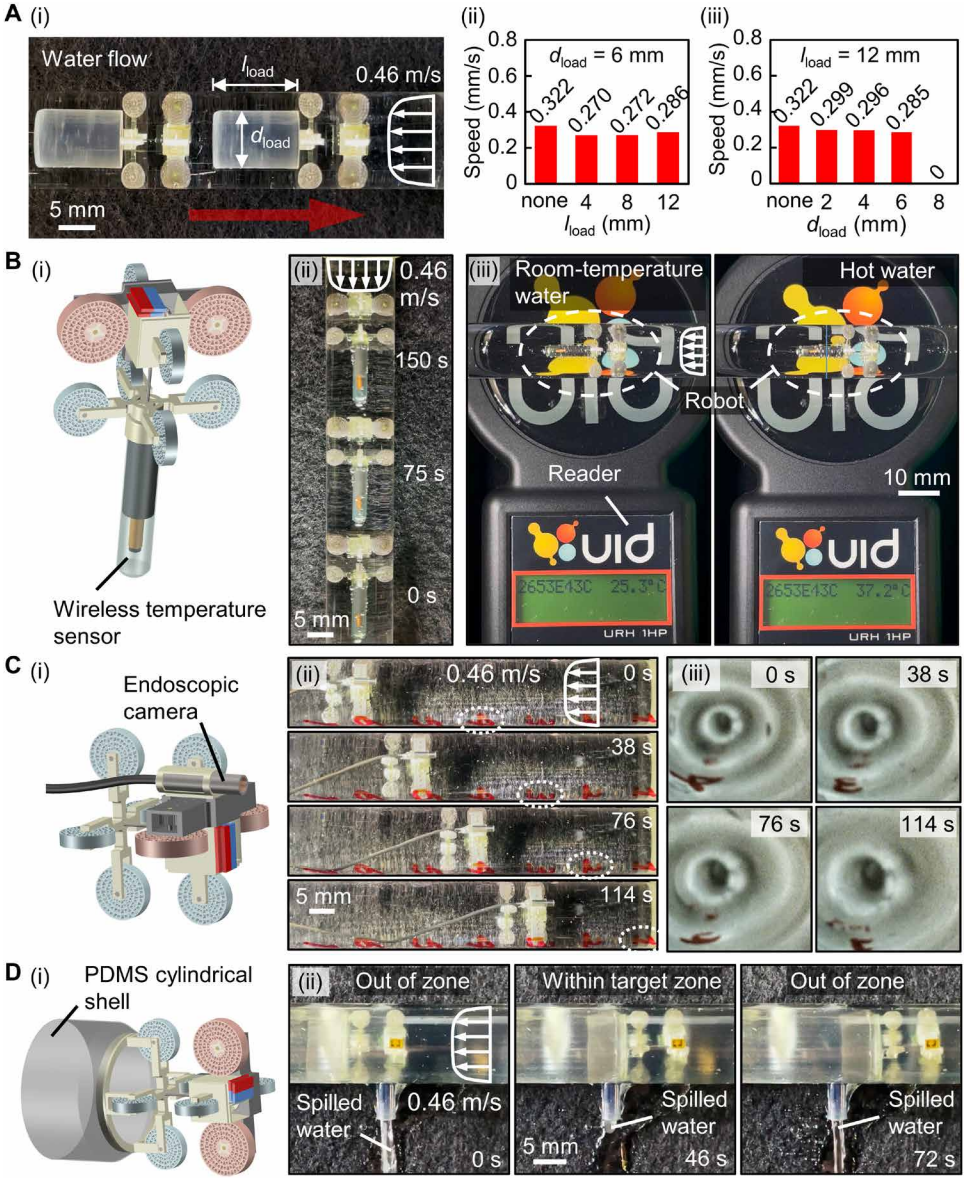

Fig. 6. Demonstration of carrying functional payloads for potential various applications. (**A**) Speed characterization of the robot with payloads of different sizes. The diameter of the pipe used for testing was 10.9 mm. (i) The robot, carrying a cylindrical load, moved against the water flow. Plots of the robot locomotion speed as functions of (ii) l_{load} and (iii) d_{load}. (**B**) Demonstration of equipping the robot with a wireless temperature sensor for flow temperature monitoring. (i) The sensor was fixed at the end of the robot. (ii) The robot can move against the flow when carrying the temperature sensor. (iii) By using an external reader, the temperature of the flowing medium can be obtained. (**C**) Demonstration of equipping the robot with an endoscopic camera for in-pipe imaging. (i) The camera was mounted on the gearbox of the robot. (ii) The robot moved against the flow in a pipe with Arabic numerals painted on the wall. (iii) Video frames captured by the onboard camera at time frames corresponding to the different robot locations in (ii). (**D**) Demonstration of equipping the robot with a soft cylindrical leak-stopper for mitigating pipeline leaks. (i) A leak-stopper made of PDMS film was mounted at the end of the robot. (ii) As the robot moved against flow and stayed near the leaking zone, the film could cover the leaking point to mitigate the liquid spray. At 46 s, the spilled water was notably reduced. Re-activating the external magnetic field to open the magnetic gate enabled the robot to leave the leaking zone.

using a handheld reader (high-powered hand-held reader URH-1HP, AnimaLab Inc.) positioned 80 mm away (Fig. 6Biii). The reader powered the sensor and acquired data wirelessly. The RF signals can transmit through liquids and most solids, with the exception of metal (*66*). However, alternative wireless sensor technologies, such as microwave-based sensors (*67*), can be suitable for metal pipelines.

The use of in-pipe mobile visual inspection is a promising method for detecting and positioning defects in pipelines, thereby promoting pipeline safety and ensuring the proper functioning of the system (*68*, *69*). By installing a nonmagnetic endoscopic camera (microendoscope camera CHS070F10F3T000, ScoutCam Inc.) next to the gearbox (Fig. 6Ci), the robot could visually capture surrounding information as it moved. As the robot moved against flow in a glass pipe with Arabic numerals on its surface, the camera sent back video capturing surface features of the pipe in real time (Fig. 6C, ii and iii and movie S13).

Pipeline leaks pose risks to natural resources, human safety, the environment, and the integrity of pipeline infrastructure (*70*, *71*). Wireless tube robots have shown promise in helping to detect and repair leaks. Here, we demonstrated that a soft cylindrical shell made of 100-μm PDMS film can be integrated with the robot to mitigate pipeline leaks (Fig. 6Di). The robot first navigated against flow inside a leaking pipe while carrying a soft cylindrical shell (Fig. 6Dii and movie S14). Once the robot reached the target area with the cylindrical shell properly positioned to cover the leak, an external magnetic field was applied to close the magnetic gates, halting the robot's movement (Fig. 6Dii). This process effectively reduced the amount of spilled water. To resume the robot's motion and move it away from the leaking zone, the external magnetic field was used to change the gate state, so that the impeller rotated again.

DISCUSSION

In this study, we demonstrated a wireless millimeter-scale wheeled robot capable of using flow energy to navigate through complex tubular structures, thereby achieving energy autonomy. A 3-mm flow-powering module—comprising an impeller, housing, and gate—was developed to efficiently convert environmental flow energy into mechanical energy. Under a load torque of 0.262 μN · m and at an average water flow rate of 1.0 m/s, this module achieved an impeller speed of 9595 rpm and generated an output power of 0.263 mW (power density of 11.69 $\mu W/mm^3$). The power density of this flow-powering module was comparable to the magnetic actuation (*62*). A dual-output miniature gearbox transformed the high-speed, low-torque impeller motion into symmetric and powerful wheel motions. The kirigami-based wheel design enabled the robot to navigate adaptively through pipes with inner diameters ranging from 10.4 to 11.4 mm and curvature radii of the center line down to 25 mm. As a result, the robot can traverse complex tubular structures of varying diameters, complex shapes (S-, U-, spiral-, and 3D-shaped pipes), and diverse materials (silicone rubber, copper, stainless steel, PVC, aluminum, glass, and polymer resin). The flow-powering module was also compatible with different flow characteristics, allowing the robot to navigate through various flow media (gases and liquids of different viscosities) and flow rates. The robot outperformed other wireless miniature tube robots in its ability to move against water flow with an average rate of up to 1.05 m/s (5.44 l/min) (*2*). By attaching magnetic gates to the housing entry, the robot's motion status can be magnetically switched between moving against flow, stopping, and moving with flow. The robot exhibited a high load capacity, enabling the integration of diverse functional payloads for tasks including endoscopic camera–based pipeline visual inspection, wireless temperature microchip–based temperature monitoring, and infrastructure maintenance with a leak-stopper shell.

Moreover, the combination of the flow-powering module and miniature gearbox offers a generic actuation solution for miniature robots to operate in flow fields. However, the current module was developed for effective actuation in water flow. For specific application scenarios, the module parameters should be optimized by considering the characteristics of the flow medium, such as cooling agents in aircraft engines and different types of oil in refineries. We envisage that this flow-powering method could be integrated with other function modules to achieve various robotic tasks in flow fields, such as liquid sampling (*62*), drug delivery (*6*), grasping (*72*), cleaning (*12*), and more. In addition, the proposed actuation method has the potential to generate electricity to power the robot's own locomotion, function, or electronic devices for sensing or data transmission, once equipped with a miniature generator, which would expand its application in the field.

Further investigation is still required for several aspects of the proposed robot. First, the anchoring force that balances flow resistance acting on the body is provided by the wheel friction force. To ensure stable locomotion in tubes with high flow rates (>1 m/s) or low-friction surfaces such as oil pipelines, streamlining the robot body to minimize flow resistance or adding microstructures to the wheel surfaces to increase friction may be effective. Second, the robot's motion status switching is limited by the working distance of external magnetic fields. To address this, future robots will be equipped with onboard miniaturized batteries, actuators (such as shape memory alloys), and microdrive and communication circuits to enable long-distance remote control. The onboard components will be used solely to enable a gate-swing motion for switching the robot's motion status, akin to an underwater glider (*73*). This approach may lead to a substantial increase in operation duration and a decrease in size.

MATERIALS AND METHODS

Design of dual-output miniature gearbox

The gearbox consists of four parts: gears, shafts, plates, and sleeves, as illustrated in fig. S1. A total of 14 gears were used to achieve flow torque amplification and motion conversion to dual outputs. The gear design parameters are listed in table S1. Gear 1 is fixed to the impeller to take over the input flow torque, and gear 6 is fixed to the shaft to output powerful rotational motion. Gear 2 has the same number of teeth as gear 1, allowing both transmission chains to produce output motion at the same speed and in opposite directions. Gears 3 to 5 are all duplex gears, which can slide freely on the shaft. The role of the sleeve is to restrict the axial movement of the gear. The gearbox has a very high reduction ratio of 2018 for each transmission chain to provide sufficient output torque for locomotion and to avoid being back-driven by the flow in the stop state. We sealed both sides of the gearbox to improve transmission efficiency and isolate contaminants.

Fabrication of the robot

The impeller and housing in the flow-powering module were fabricated by two-photon polymerization with negative-tone photoresist

(IP-Q, Nanoscribe GmbH) (Fig. 2C). The magnetic gate for tuning impeller rotation state was fabricated in three steps: First, uncured PDMS (precursor to curing agent mass ratio of 10:1; Sylgard 184, Dow Corning) was mixed with NdFeB magnetic particles (5-μm average diameter; MQP-15-7, Magnequench) with a 1:4 mass ratio and flattened by a razor blade to form a 0.3-mm-thick layer. After curing at 90°C for 2 hours, the gate-shaped pieces were cut out with a laser cutter (LPFK ProtoLaser U3). The gate pieces were then magnetized using a vibrating sample magnetometer (VSM; EZ7, MicroSense) at a uniform magnetic field of 1.8 T.

For the miniature gearbox, gears and plates were fabricated through mold casting (*62*). First, part-featured positive molds were fabricated on silicon wafers by two-photon polymerization with negative-tone photoresist (IP-S, Nanoscribe GmbH). To facilitate the demolding process, these molds were silanized by trichloro(1*H*,1*H*,2*H*,2*H*-perfluorooctyl) silane 97% (Merck KGaA). To make negative molds, uncured PDMS (precursor to curing agent mass ratio of 10:1; Sylgard 184, Dow Corning) was cast onto the silanized positive molds followed by vacuum degassing and 2-hour curation at 90°C. The negative molds were taken out and silanized. An uncured epoxy resin (EpoxAcast 655, Smooth-On) was cast into the negative molds followed by vacuum degassing. The excessive resin above the mold surface was scraped off with a razor blade. After 12 hours of curing at 23°C and 3 hours of heat curing at 80°C, the parts were taken out with a tweezer. Parts made from this aluminum-filled resin have the advantages of low friction and high strength. Sleeves were fabricated by two-photon polymerization with IP-S photoresist. Shafts with different diameters were made of brass rods (0.3 mm in diameter; BW03, Albion Alloys) and acupuncture needles (0.12, 0.14, and 0.2 mm in diameter; S-J1215, S-J1415, and S-J2030, Seirin Corporation).

The kirigami wheels made of PDMS (precursor to curing agent mass ratio of 10:1; Sylgard 184, Dow Corning) were fabricated by mold casting. The wheel holders were fabricated by two-photon polymerization with IP-Q photoresist. The robot assembly was conducted under a stereomicroscope (ZEISS Stemi 508, Carl Zeiss Microscopy GmbH). During robot assembly, bonding agents were applied between the parts to ensure a robust connection. Cyanoacrylate adhesive (Loctite 495) was applied between most parts, such as between the housing and the gearbox and between the impeller and the shaft. In addition, dimethacrylate adhesive (Loctite 601) was used between the gears and the output shafts.

Simulation of the flow-powering module

Finite element method (FEM) simulation was used to estimate the energy conversion performance of the impeller with various designs in turbulent water flows. Using a commercial FEM tool (COMSOL Multiphysics 6.0, COMSOL Inc.), the angular velocity of the impeller was estimated on the basis of the rotating machinery, turbulent flow interface. We assumed that the inlet flow followed the Reynolds-averaged Navier-Stokes model ($k-\varepsilon$), where k and ε represent the turbulent kinetic energy and the turbulent dissipation rate, respectively, within the model (*63*), and had a fully developed velocity profile estimated by the COMSOL turbulent flow, $k-\varepsilon$ interface while ignoring the influence of the robot body on the flow. Because the impeller was small relative to the tube diameter and located in the central region, the flow velocity variation in the impeller's axial direction was neglected, so that the model could be reduced to a 2D configuration (Fig. 2B and fig. S2A). We used the cross section of the impeller in the tube at the middle layer of the impeller as the effective 2D problem. The effective tube diameter was 10.29 mm, and the inlet flow profile at the left bound was calculated on the basis of the average flow rate in the tube. The outlet flow at the right bound was set to be 0-Pa pressure. The impeller together with the surrounding walls of the housing was positioned in the middle of the tube. The walls were fixed rigid bounds, whereas the fins of the impeller were free to rotate around its center. To consider the effect of the load torque from the robot, a torque of prescribed various values was applied to the impeller in a CW direction, as denoted using a blue circle arrow in Fig. 2B. The fluid domain was set as water, and the Yeoh method with a stiffening factor of 10 was used for mesh smoothing in deformation. The problem was solved for a duration of 0.1 s with a time step of 0.0005 s. To enhance convergence, the inlet flow and load torque were smoothly ramped up to full amounts within the first 0.025 s using default ramp functions, $u_{\text{flow}}(x, y, t)$ and $T_{\text{load}}(t)$. Because the rotation of the fins caused large fluid mesh deformation, a remeshing tool was used to ensure successful completion of the computation.

The impeller's design parameters—such as the amount, length, and thickness of the fins and the gap between the fins and walls—were investigated through the simulation model. The effects of the flow rate and load torque were also analyzed using the model. The mean impeller rotational speed $\overline{n_{\text{i}}}$ over one cycle during the steady state was used to evaluate the impeller's performance (fig. S2C).

The impeller output power P_{out}, the flow power at the housing inlet P_{inflow}, and the flow power at the housing outlet P_{outflow} can be calculated as

$$P_{\text{out}} = \frac{2\pi n_{\text{i}}}{60} \cdot T_{\text{load}} \tag{5}$$

$$P_{\text{inflow}} = \int_{A_{\text{front}}} p \cdot \mathbf{u}_{\text{flow}} \cdot \mathbf{n}_{\text{A}} \cdot dA \tag{6}$$

$$P_{\text{outflow}} = \int_{A_{\text{rear}}} p \cdot \mathbf{u}_{\text{flow}} \cdot \mathbf{n}_{\text{A}} \cdot dA \tag{7}$$

where p, $\mathbf{u}_{\text{flow}}$, and $\mathbf{n}_{\text{A}}$ denote the pressure, flow velocity vector, and unit vector normal to the unit surface area dA, respectively. A_{front} and A_{rear} denote the surface areas of the front and rear openings of the housing (Fig. 2Fi).

The energy conversion efficiency η was calculated as the ratio between mean output power and mean flow power passing through the housing

$$\eta = \frac{\overline{P_{\text{out}}}}{\overline{P_{\text{inflow}}} - \overline{P_{\text{outflow}}}} \tag{8}$$

where $\overline{P}$ is the mean power over one rotational cycle of the impeller under the steady state.

Characterization of the flow-powering module

The impeller housing for characterization was mounted inside a straight glass pipe (fig. S3A). A membrane hydraulic pump (Xylem

Flojet R352) was used to generate the controllable flow rate in the tube. The pipe flow rate at different drive voltages of the pump was calibrated by a flow sensor (Iduino TC-9520276). The impeller motion was captured with a high-speed camera at a frame rate of 5000 fps. To apply a controllable load torque on the impeller, we mounted a friction disk with an axially magnetized disc magnet on the impeller shaft (fig. S3A) and mounted the other disc permanent magnet (20 mm in diameter and height, Supermagnete) on a two–degree-of-freedom (two-DOF) linear translation stage (two-axis configurations of XR50C/M and XR25C, Thorlabs). By precisely adjusting the stage to make the two magnets coaxial and controlling the distance between them, the magnetic gradient force F_g applied to the friction disk could be modulated. Thus, the load torque T_{load} on the impeller could be controlled

$$T_{load} = \mu_d F_g r_f \tag{9}$$

where μ_d is the friction coefficient between the friction disk and the plate and r_f is the radius of the friction circle (fig. S3A). Because F_g was constant for different rotation angles of the friction disk, the load torque on the impeller was considered to be constant as the impeller rotates. The plate and the friction disk were fabricated through mold casting with an epoxy resin (EpoxAcast 655, Smooth-On) because of their high surface hardness, so μ_d was determined to be 0.11 ± 0.01 (*62*). The disc magnet on the friction disk was fabricated by mold casting, and it had a magnetization of 300 kA/m measured with a VSM. The magnetic gradient force F_g between the two magnets at different distances was then investigated by magnetostatic field simulation in COMSOL Multiphysics (fig. S3, B and C).

Simulation of the kirigami wheels

To evaluate the performance of the designed kirigami wheels affected by different factors, we performed a numerical study of the mechanical performance of the kirigami wheels when rolling under compression using ABAQUS/Standard finite element software (Fig. 3B). The 3D static contact model was simplified as a rigid plate compressing a soft wheel vertically and then translating horizontally.

The soft wheel was modeled as a nonlinear hyperelastic material with geometrical nonlinearity. The hyperelastic constitutive model and material parameters of PDMS were determined by the stress-strain curve obtained from the uniaxial test (*74*) and are listed in table S2. The wheel and plate were meshed using the linear hybrid hexahedral elements (C3D8RH) with a global element size of 0.02 mm. The contact between the wheel and the plate was implemented using the penalty-based surface-to-surface interactions with a friction coefficient of 0.2 and a normal hard contact property. For the wheel interior surface, a frictionless self-contact algorithm was considered to avoid self-penetration at large deformations.

Figure 3B shows the boundary conditions of the geometry model, where the plate was constrained by a control point (RF_1) as a rigid body. The other reference point (RF_2) located at the center of mass of the wheel was kinematic coupled to the inner surface of the wheel. A compression displacement Δy was applied to the y-axis translational DOF, and a displacement Δx was added to the x axis translational DOF of the plate. The rotational DOF around the wheel's z axis was released.

At the first analysis step with shorter time periods, Δy was gradually increased from 0 to 0.01 mm to establish a smooth contact for improving contact convergence. In step 2, a compression displacement Δy was applied, gradually increasing from 0.01 mm to a target value. In the next step, the translational displacement Δx was set to ramp up from 0 to the circumference of the wheel. Considering the nonlinear effects of the large deformation, the full-Newton algorithm was used for implicit time integration in the static analysis.

The η_{wheel} of the F_n during a wheel rotation cycle was calculated as follows

$$\eta_{wheel} = \mathrm{RMSD} / \overline{F_n} \tag{10}$$

where RMSD is the root mean square deviation. Furthermore, RMSD can be defined as

$$\mathrm{RMSD} = \sqrt{\frac{1}{N}\sum_{i=1}^{N}(F_{ni} - \overline{F_n})^2} \tag{11}$$

where F_{ni} is the output compression force at the time instant i and N is the total number of the discretized time instants in a wheel rotation cycle.

In-pipe force analysis of the robot

During slip-free locomotion, fluid drag force F_{flow} was balanced by the traction force F_t from both active wheels, with negligible contribution from the passive wheels due to their rotational freedom (fig. S5A). Assuming symmetrical deformation of active wheels in a straight pipeline, F_t equaled $0.5F_{flow}$. To prevent active wheel-pipe wall slippage, each active wheel's maximum friction force must exceed F_t, which gives

$$\mu_w F_n > 0.5 F_{flow} \tag{12}$$

where μ_w is the friction coefficient between wheel surface and pipe wall and F_n is the normal force from each active wheel.

The value of μ_w was influenced by the wheel and pipe wall materials, as well as the surrounding fluid medium. Enhanced slip-free locomotion was facilitated by higher values of μ_w. Submerged conditions yield $\mu_w > 0.7$ between PDMS (the high-friction material adopted by wheels) and various materials in the presence of water (*60*, *61*). F_{flow} increased with the increasing v_{flow}, whereas the robot shape, pipe diameter, and flow properties remained constant. Higher F_{flow} values posed a risk of slippage. F_n relied on the kirigami wheel materials, configuration parameters (p_t, p_d, p_n), and the compression Δy of the wheels (Fig. 3).

To analyze the exerted F_{flow} on the robot, we conducted simulations using COMSOL Multiphysics 6.0 (fig. S5B). A physical entity with characteristics matching the robot's shape was used for simulation. A uniform flow velocity profile was set at the pipe entrance, gradually developing into a suitable flow field over a 200-mm distance before reaching the robot. The integration of pressures across the robot's surfaces yielded the total F_{flow} that it experienced.

Characterization of the kirigami wheels

The compression mechanics of the kirigami wheels during rolling were characterized using a customized setup (fig. S6). The wheel was mounted on a 3D-printed holder (IP-S, NanoScribe), which was connected to two load cells (GSO-25, Transducer Techniques LLC, and LSB200, FUTEK Inc.) to measure normal and tangential forces. The load cells were attached to a vertical linear motor stage (LTS150/M, Thorlabs Inc.). A glass slide was fixed on a lateral linear motor stage (LTS150/M, Thorlabs Inc.). The rolling test involved loading and dragging steps. First, the wheel was loaded onto the

glass slide at a depth of 0.2 or 0.35 mm through vertical translation by the vertical linear motor. Then, the lateral linear motor and glass slide moved horizontally for 14 mm (over one revolution of wheel rotation) during the dragging step. The loading and dragging speeds were set to 50 μm/s. Each test was repeated five times.

Supplementary Materials

This PDF file includes:
Tables S1 and S2
Figs. S1 to S10

Other Supplementary Material for this manuscript includes the following:
Movies S1 to S14
MDAR Reproducibility Checklist

REFERENCES AND NOTES

1. C. Tang, B. du, S. Jiang, Q. Shao, X. Dong, X. J. Liu, H. Zhao, A pipeline inspection robot for navigating tubular environments in the sub-centimeter scale. *Sci. Robot.* **7**, eabm8597 (2022).
2. T. Wang, H. Ugurlu, Y. Yan, M. Li, M. Li, A. M. Wild, E. Yildiz, M. Schneider, D. Sheehan, W. Hu, M. Sitti, Adaptive wireless millirobotic locomotion into distal vasculature. *Nat. Commun.* **13**, 4465 (2022).
3. U. Bozuyuk, Y. Alapan, A. Aghakhani, M. Yunusa, M. Sitti, Shape anisotropy-governed locomotion of surface microrollers on vessel-like microtopographies against physiological flows. *Proc. Natl. Acad. Sci.* **118**, e2022090118 (2021).
4. Y. Wu, X. Dong, J.-K. Kim, C. Wang, M. Sitti, Wireless soft millirobots for climbing three-dimensional surfaces in confined spaces. *Sci. Adv.* **8**, eabn3431 (2022).
5. H.-J. Yoon, G. Lee, J. T. Kim, J. Y. Yoo, H. Luan, S. Cheng, S. Kang, H. L. T. Huynh, H. Kim, J. Park, J. Kim, S. S. Kwak, H. Ryu, J. Kim, Y. S. Choi, H. Y. Ahn, J. Choi, S. Oh, Y. H. Jung, M. Park, W. Bai, Y. Huang, L. P. Chamorro, Y. Park, J. A. Rogers, Biodegradable, three-dimensional colorimetric fliers for environmental monitoring. *Sci. Adv.* **8**, eade3201 (2022).
6. S. S. Srinivasan, A. Alshareef, A. V. Hwang, Z. Kang, J. Kuosmanen, K. Ishida, J. Jenkins, S. Liu, W. A. M. Madani, J. Lennerz, A. Hayward, J. Morimoto, N. Fitzgerald, R. Langer, G. Traverso, RoboCap: Robotic mucus-clearing capsule for enhanced drug delivery in the gastrointestinal tract. *Sci. Robot.* **7**, eabp9066 (2022).
7. S. Song, S. Yuan, F. Zhang, J. Su, D. Ye, J. Wang, M. Q.-H. Meng, Integrated design and decoupled control of anchoring and drug release for wireless capsule robots. *IEEE/ASME Trans. Mechatron.* **27**, 2897–2907 (2022).
8. S. I. Rich, R. J. Wood, C. Majidi, Untethered soft robotics. *Nat. Electron.* **1**, 102–112 (2018).
9. B. H. Kim, K. Li, J. T. Kim, Y. Park, H. Jang, X. Wang, Z. Xie, S. M. Won, H. J. Yoon, G. Lee, W. J. Jang, K. H. Lee, T. S. Chung, Y. H. Jung, S. Y. Heo, Y. Lee, J. Kim, T. Cai, Y. Kim, P. Prasopsukh, Y. Yu, X. Yu, R. Avila, H. Luan, H. Song, F. Zhu, Y. Zhao, L. Chen, S. H. Han, J. Kim, S. J. Oh, H. Lee, C. H. Lee, Y. Huang, L. P. Chamorro, Y. Zhang, J. A. Rogers, Three-dimensional electronic microfliers inspired by wind-dispersed seeds. *Nature* **597**, 503–510 (2021).
10. B. J. Nelson, I. K. Kaliakatsos, J. J. Abbott, Microrobots for minimally invasive medicine. *Annu. Rev. Biomed. Eng.* **12**, 55–85 (2010).
11. M. Sitti, Miniature soft robots—road to the clinic. *Nat. Rev. Mater.* **3**, 74–75 (2018).
12. W.-K. Lee, D. J. Preston, M. P. Nemitz, A. Nagarkar, A. K. MacKeith, B. Gorissen, N. Vasios, V. Sanchez, K. Bertoldi, L. Mahadevan, G. M. Whitesides, A buckling-sheet ring oscillator for electronics-free, multimodal locomotion. *Sci. Robot.* **7**, eabg5812 (2022).
13. Y. Kim, G. A. Parada, S. Liu, X. Zhao, Ferromagnetic soft continuum robots. *Sci. Robot.* **4**, eaax7329 (2019).
14. F. Connolly, P. Polygerinos, C. J. Walsh, K. Bertoldi, Mechanical programming of soft actuators by varying fiber angle. *Soft Robot.* **2**, 26–32 (2015).
15. M. S. Verma, A. Ainla, D. Yang, D. Harburg, G. M. Whitesides, A soft tube-climbing robot. *Sci. Robot.* **5**, 133–137 (2018).
16. J. A.-C. Liu, J. H. Gillen, S. R. Mishra, B. A. Evans, J. B. Tracy, Photothermally and magnetically controlled reconfiguration of polymer composites for soft robotics. *Sci. Adv.* **5**, eaaw2897 (2019).
17. L. Ren, N. Nama, J. M. McNeill, F. Soto, Z. Yan, W. Liu, W. Wang, J. Wang, T. E. Mallouk, 3D steerable, acoustically powered microswimmers for single-particle manipulation. *Sci. Adv.* **5**, eaax3084 (2019).
18. Z. Ren, R. Zhang, R. H. Soon, Z. Liu, W. Hu, P. R. Onck, M. Sitti, Soft-bodied adaptive multimodal locomotion strategies in fluid-filled confined spaces. *Sci. Adv.* **7**, eabh2022 (2021).
19. W. Hu, G. Z. Lum, M. Mastrangeli, M. Sitti, Small-scale soft-bodied robot with multimodal locomotion. *Nature* **554**, 81–85 (2018).
20. Y. Wang, M. Li, J. K. Chang, D. Aurelio, W. Li, B. J. Kim, J. H. Kim, M. Liscidini, J. A. Rogers, F. G. Omenetto, Light-activated shape morphing and light-tracking materials using biopolymer-based programmable photonic nanostructures. *Nat. Commun.* **12**, 1651 (2021).
21. A. Aghakhani, O. Yasa, P. Wrede, M. Sitti, Acoustically powered surface-slipping mobile microrobots. *Proc. Natl. Acad. Sci.* **117**, 3469–3477 (2020).
22. A. Kotikian, C. McMahan, E. C. Davidson, J. M. Muhammad, R. D. Weeks, C. Daraio, J. A. Lewis, Untethered soft robotic matter with passive control of shape morphing and propulsion. *Sci. Robot.* **4**, eaax7044 (2019).
23. T. Chen, O. R. Bilal, K. Shea, C. Daraio, Harnessing bistability for directional propulsion of soft, untethered robots. *Proc. Natl. Acad. Sci.* **115**, 5698–5702 (2018).
24. Z. Zhakypov, K. Mori, K. Hosoda, J. Paik, Designing minimal and scalable insect-inspired multi-locomotion millirobots. *Nature* **571**, 381–386 (2019).
25. M. Wang, D. Vecchio, C. Wang, A. Emre, X. Xiao, Z. Jiang, P. Bogdan, Y. Huang, N. A. Kotov, Biomorphic structural batteries for robotics. *Sci. Robot.* **5**, eaba1912 (2020).
26. A. E. Holness, A. Perez-Rosado, H. A. Bruck, M. Peckerar, S. K. Gupta, *Challenges in Mechanics of Time Dependent Materials*, in *Proceedings of the 2016 Annual Conference on Experimental and Applied Mechanics* (Springer, 2017), vol. 2, pp. 155–162.
27. C. A. Aubin, S. Choudhury, R. Jerch, L. A. Archer, J. H. Pikul, R. F. Shepherd, Electrolytic vascular systems for energy-dense robots. *Nature* **571**, 51–57 (2019).
28. C. A. Aubin, B. Gorissen, E. Milana, P. R. Buskohl, N. Lazarus, G. A. Slipher, C. Keplinger, J. Bongard, F. Iida, J. A. Lewis, R. F. Shepherd, Towards enduring autonomous robots via embodied energy. *Nature* **602**, 393–402 (2022).
29. Y. Alapan, U. Bozuyuk, P. Erkoc, A. C. Karacakol, M. Sitti, Multifunctional surface microrollers for targeted cargo delivery in physiological blood flow. *Sci. Robot.* **5**, eaba5726 (2020).
30. J. Li, I. Rozen, J. Wang, Rocket science at the nanoscale. *ACS Nano* **10**, 5619–5634 (2016).
31. W. Gao, J. Wang, Synthetic micro/nanomotors in drug delivery. *Nanoscale* **6**, 10486–10494 (2014).
32. J. M. M. Tur, W. Garthwaite, Robotic devices for water main in-pipe inspection: A survey. *J. Field Robot.* **4**, 491–508 (2010).
33. T. Idogaki, H. Kanayama, N. Ohya, H. Suzuki, T. Hattori, Characteristics of piezoelectric locomotive mechanism for an in-pipe micro inspection machine, in *Proceedings of the Sixth International Symposium on Micro Machine and Human Science* (IEEE, 1995), pp. 193–198.
34. B. Kim, M. G. Lee, Y. P. Lee, Y. Kim, G. Lee, An earthworm-like micro robot using shape memory alloy actuator. *Sens. Actuators A Phys.* **125**, 429–437 (2006).
35. T. Zheng, X. Wang, H. Li, C. Zhao, Z. Jiang, Q. Huang, M. Ceccarelli, Design of a robot for inspecting the multishape pipeline systems. *IEEE/ASME Trans. Mechatron.* **27**, 4608–4618 (2022).
36. S.-g. Roh, H. R. Choi, Differential-drive in-pipe robot for moving inside urban gas pipelines. *IEEE Trans. Robot.* **21**, 1–17 (2005).
37. Y.-S. Kwon, B.-J. Yi, Design and motion planning of a two-module collaborative indoor pipeline inspection robot. *IEEE Trans. Robot.* **28**, 681–696 (2012).
38. E. Dertien, S. Stramigioli, K. Pulles, Development of an inspection robot for small diameter gas distribution mains, in *2011 IEEE International Conference on Robotics and Automation* (IEEE, 2011), pp. 5044–5049.
39. H. M. Kim, Y. S. Choi, Y. G. Lee, H. R. Choi, Novel mechanism for in-pipe robot based on a multiaxial differential gear mechanism. *IEEE/ASME Trans. Mechatron.* **22**, 227–235 (2017).
40. A. Kakogawa, T. Nishimura, S. Ma, Designing arm length of a screw drive in-pipe robot for climbing vertically positioned bent pipes. *Robotica* **34**, 306–327 (2016).
41. A. Kakogawa, S. Ma, in A multi-link in-pipe inspection robot composed of active and passive compliant joints, in *2020 IEEE/RSJ International Conference on Intelligent Robots and Systems (IROS)* (IEEE, 2020), pp. 6472–6478.
42. P. Debenest, M. Guarnieri, S. Hirose, PipeTron series—Robots for pipe inspection, in *Proceedings of the 2014 3rd International Conference on Applied Robotics for the Power Industry* (IEEE, 2014), pp. 1–6.
43. A. A. Calderón, J. C. Ugalde, J. C. Zagal, N. O. Pérez-Arancibia, Design, fabrication and control of a multi-material-multi-actuator soft robot inspired by burrowing worms, in *2016 IEEE International Conference on Robotics and Biomimetics (ROBIO)* (IEEE, 2016), pp. 31–38.
44. H. Takeshima, T. Takayama, Six-braided tube in-pipe locomotive device, in *2015 IEEE/RSJ International Conference on Intelligent Robots and Systems (IROS)* (IEEE, 2015), pp. 1125–1130.
45. Z. Zhang, X. Wang, S. Wang, D. Meng, B. Liang, Design and modeling of a parallel-pipe-crawling pneumatic soft robot. *IEEE Access* **7**, 134301–134317 (2019).
46. B. Zhang, Y. Fan, P. Yang, T. Cao, H. Liao, Worm-like soft robot for complicated tubular environments. *Soft Robotics* **6**, 399–413 (2019).
47. M. Ikeuchi, T. Nakamura, D. Matsubara, Development of an in-pipe inspection robot for narrow pipes and elbows using pneumatic artificial muscles, in *2012 IEEE/RSJ International Conference on Intelligent Robots and Systems* (IEEE, 2012), pp. 926–931.
48. R. Ishikawa, T. Tomita, Y. Yamada, T. Nakamura, Development of a peristaltic crawling robot for long-distance complex line sewer pipe inspections,in *2016 IEEE International Conference on Advanced Intelligent Mechatronics (AIM)* (IEEE, 2016), pp. 413–418.

49. J.-H. Kim, G. Sharma, S. S. Iyengar, FAMPER: A fully autonomous mobile robot for pipeline exploration, in *2010 IEEE International Conference on Industrial Technology* (IEEE, 2010), pp. 517–523.
50. Y. Wu, A. Noel, D. D. Kim, K. Youcef-Toumi, R. Ben-Mansour, Design of a maneuverable swimming robot for in-pipe missions, in *2015 IEEE/RSJ International Conference on Intelligent Robots and Systems (IROS)* (IEEE, 2015), pp. 4864–4871.
51. C. Ye, L. Liu, X. Xu, J. Chen, Development of an in-pipe robot with two steerable driving wheels, in *2015 IEEE International Conference on Mechatronics And Automation (ICMA)* (IEEE, 2015), pp. 1955–1959.
52. J. J. Park, J. W. Moon, H. Kim, S. C. Jang, D. G. Kim, K. Ahn, S. M. Ryew, H. Moon, H. R. Choi, Development of the untethered in-pipe inspection robot for natural gas pipelines, in *2013 10th International Conference on Ubiquitous Robots and Ambient Intelligence (URAI)* (IEEE, 2013), pp. 55–58.
53. D. Mishra, K. K. Agrawal, A. Abbas, R. Srivastava, R. Yadav, PIG [pipe inspection gauge]: An artificial dustman for cross country pipelines. *Procedia Comput. Sci.* **152**, 333–340 (2019).
54. A. Ramirez-Martinez, N. A. Rodríguez-Olivares, S. Torres-Torres, G. Ronquillo-Lomelí, J. A. Soto-Cajiga, Design and validation of an articulated sensor carrier to improve the automatic pipeline inspection. *Sensors (Basel)* **19**, 1394 (2019).
55. B. Mao, Y. Lu, P. Wu, B. Mao, P. Li, Signal processing and defect analysis of pipeline inspection applying magnetic flux leakage methods. *Intel. Serv. Robot.* **7**, 203–209 (2014).
56. Z. Hu, E. Appleton, Dynamic characteristics of a novel self-drive pipeline pig. *IEEE Trans. Robot.* **21**, 781–789 (2005).
57. J. Okamoto Jr., J. C. Adamowski, M. S. Tsuzuki, F. Buiochi, C. S. Camerini, Autonomous system for oil pipelines inspection. *Mechatronics* **9**, 731–743 (1999).
58. S. Liu, S. Liu, H. Xiao, Optimization of structural parameters of jet end in the underwater intelligent pigging robot. *Ocean Eng.* **216**, 108092 (2020).
59. A. Toffolo, A. Lazzaretto, A. Martegani, Cross-flow fan design guidelines for multi-objective performance optimization. *Proc. Inst. Mech. Eng. Part A: J. Power Energy* **218**, 33–42 (2004).
60. S.-J. Lee, Y.-C. Sohn, C.-L. Kim, Friction and wear characteristics of polydimethylsiloxane under water-based lubrication conditions. *Materials (Basel)* **15**, 3262 (2022).
61. J. Li, F. Zhou, X. Wang, Modify the friction between steel ball and PDMS disk under water lubrication by surface texturing. *Meccanica* **46**, 499–507 (2011).
62. C. Hong, Z. Ren, C. Wang, M. Li, Y. Wu, D. Tang, W. Hu, M. Sitti, Magnetically actuated gearbox for the wireless control of millimeter-scale robots. *Sci. Robot.* **7**, eabo4401 (2022).
63. P. K. Kundu, I. M. Cohen, D. R. Dowling, *Fluid Mechanics* (Academic Press, 2015).
64. M. A. Alanazi, T. E. Diller, New non-invasive thermal sensor design for a pipe flow. *Therm. Sci. Eng. Prog.* **29**, 101238 (2022).
65. H. Huan, L. Liu, X. Chen, C. Peng, J. Zhan, Q. Liu, Y. Yao, An indirect temperature measurement of oil pipelines based on embedded devices. *Measurement* **159**, 107747 (2020).
66. C. Coleman, *An Introduction to Radio Frequency Engineering* (IET, 2012).
67. C. Mätzler, *Thermal Microwave Radiation: Applications for Remote Sensing* (IET, 2006), vol. 52.
68. T. Takayama, H. Takeshima, T. Hori, T. Omata, A twisted bundled tube locomotive device proposed for in-pipe mobile robot. *IEEE/ASME Trans. Mechatron.* **20**, 2915–2923 (2015).
69. A. Verma, A. Kaiwart, N. D. Dubey, F. Naseer, S. Pradhan, A review on various types of in-pipe inspection robot. *Mater. Today Proc.* **50**, 1425–1434 (2022).
70. D. Chatzigeorgiou, K. Youcef-Toumi, R. Ben-Mansour, Design of a novel in-pipe reliable leak detector. *IEEE/ASME Trans. Mechatron.* **20**, 824–833 (2015).
71. H. Lu, T. Iseley, S. Behbahani, L. Fu, Leakage detection techniques for oil and gas pipelines: State-of-the-art. *Tunn. Undergr. Space Technol.* **98**, 103249 (2020).
72. N. R. Sinatra, C. B. Teeple, D. M. Vogt, K. K. Parker, D. F. Gruber, R. J. Wood, Ultragentle manipulation of delicate structures using a soft robotic gripper. *Sci. Robot.* **4**, eaax5425 (2019).
73. D. L. Rudnick, R. E. Davis, C. C. Eriksen, D. M. Fratantoni, M. J. Perry, Underwater gliders for ocean research. *Mar. Technol. Soc. J.* **38**, 73–84 (2004).
74. F. Hajiali, A. Shojaei, Network structure and mechanical properties of polydimethylsiloxane filled with nanodiamond–Effect of degree of silanization of nanodiamond. *Compos. Sci. Technol.* **142**, 227–234 (2017).

Acknowledgments: We thank N. Krishna-Subbaiah and A. Shiva for assistance in experiments and M. E. Tiryaki for discussions on endoscopic imaging. **Funding:** This work was funded by the Max Planck Society, European Research Council (ERC) Advanced Grant SoMMoR project grant no. 834531 and German Research Foundation (DFG) Soft Material Robotic Systems (SPP 2100) Program grant no. 2197/3-1. C.H. thanks the China Scholarship Council (grant no. 202006120160) for financial support. Y.W. thanks the National Natural Science Foundation of China (grant no. 52125505) and the Alexander von Humboldt Foundation for financial support. W.H. thanks startup funding and the Department of Mechanical and Aerospace Engineering from Hong Kong University of Science and Technology. **Author contributions:** C.H., Y.W., W.H., and M.S. conceived the idea and designed the research. C.H. and Y.W. performed the experiments and analyzed the data with the help of Z.R., Chunxiang Wang, and Z.L. Y.W., Che Wang, and C.H. performed simulations. M.S. and W.H. supervised the research. The manuscript was written by C.H., Y.W., W.H., and M.S. with input from all authors. All authors discussed the results and commented or edited the manuscript. **Competing interests:** The authors declare that they have no competing financial interests. **Data and materials availability:** All data needed to evaluate the conclusions in the paper are presented in the paper and the Supplementary Materials and are available online at https://doi.org/10.5061/dryad.mw6m90648.

Submitted 2 May 2023
Accepted 13 February 2024
Published 13 March 2024
10.1126/scirobotics.adi5155